AGU PUBLICATIONS

Geophysical Research Letters

RESEARCH LETTER
10.1002/2017GL073159

Special Section:
Early Results: Juno at Jupiter

The distribution of ammonia on Jupiter from a preliminary inversion of Juno microwave radiometer data

Cheng Li[1], Andrew Ingersoll[2], Michael Janssen[1], Steven Levin[1], Scott Bolton[3], Virgil Adumitroaie[1], Michael Allison[4], John Arballo[1], Amadeo Bellotti[5], Shannon Brown[1], Shawn Ewald[2], Laura Jewell[1], Sidharth Misra[1], Glenn Orton[1], Fabiano Oyafuso[1], Paul Steffes[5], and Ross Williamson[1]

[1]Jet Propulsion Laboratory, California Institute of Technology, Pasadena, California, USA, [2]California Institute of Technology, Pasadena, California, USA, [3]Southwest Research Institute, San Antonio, Texas, USA, [4]Goddard Institute for Space Studies, New York, New York, USA, [5]Georgia Institute of Technology, Atlanta, Georgia, USA

Key Points:
- Jupiter's deep ammonia abundance is estimated using nadir brightness temperatures
- Ammonia gas concentration is depleted with respect to the deep value down to at least 50 bars outside of the Equatorial Zone
- An ammonia-rich zone occupies 0-5°N and extends from the deep atmosphere to the base of the ammonia cloud.

Correspondence to:
C. Li,
cli@gps.caltech.edu

Citation:
Li, C., et al. (2017), The distribution of ammonia on Jupiter from a preliminary inversion of Juno microwave radiometer data, *Geophys. Res. Lett.*, *44*, 5317–5325, doi:10.1002/2017GL073159.

Received 20 FEB 2017
Accepted 15 MAY 2017
Accepted article online 25 MAY 2017
Published online 3 JUN 2017

Abstract The Juno microwave radiometer measured the thermal emission from Jupiter's atmosphere from the cloud tops at about 1 bar to as deep as a hundred bars of pressure during its first flyby over Jupiter (PJ1). The nadir brightness temperatures show that the Equatorial Zone is likely to be an ideal adiabat, which allows a determination of the deep ammonia abundance in the range 362^{+33}_{-33} ppm. The combination of Markov chain Monte Carlo method and Tikhonov regularization is studied to invert Jupiter's global ammonia distribution assuming a prescribed temperature profile. The result shows (1) that ammonia is depleted globally down to 50–60 bars except within a few degrees of the equator, (2) the North Equatorial Belt is more depleted in ammonia than elsewhere, and (3) the ammonia concentration shows a slight inversion starting from about 7 bars to 2 bars. These results are robust regardless of the choice of water abundance.

Plain Language Summary The distribution of ammonia gas on Jupiter's atmosphere was derived by fitting the microwave spectra measured by the Juno spacecraft. The result showed that the concentration of ammonia gas in the extratropics was much less than expected and had a local minimum near 7 bars of pressure.

1. Introduction

On 27 August 2016, the Juno spacecraft traveled between Jupiter's synchrotron radiation belt and the planetary disk. During perijove, the microwave radiometer (MWR) onboard the spacecraft measured the thermal radiation from the atmosphere at wavelengths up to 50 cm, which originates from depths reaching down to pressures of a few hundred bars [*Bolton et al.*, 2017]. The observed brightness temperatures at six microwave channels reveal the global abundance of ammonia and the dynamical features in the deep atmosphere. Here we report on the preliminary result and how it was achieved. We focus on ammonia because it is the main opacity source, and the deep features show up readily in the data, even if we restrict our analysis to nadir views. Water shows up best in off-nadir views, that is, in the limb darkening, and those data have not been fully analyzed. Thus, the main product of the present analysis is the deep ammonia abundance as well as a two-dimensional cross section (vertical and latitudinal) of the ammonia distribution.

In section 2, we begin with a qualitative description of the observed antenna temperatures. An immediate conclusion is that Jupiter's atmosphere is close to an ideal adiabat only within a few degrees near the equator. In section 3, we introduce the retrieval algorithm, a Markov chain Monte Carlo simulation with Tikhonov regularization, that quantitatively inverts the radiances to yield the global distribution of ammonia. Why a regularization term is needed and how to design it are explained. Both the deep ammonia abundance and the distribution of ammonia are derived from this method. Finally, we summarize our conclusions and emphasize how to interpret them correctly in section 4.

2. Qualitative Description of the Data

The Juno MWR measures the thermal emission of Jupiter's atmosphere at six wavelengths and multiple emission angles, expressed in brightness temperature (T_b). Due to the finite beam size of the antenna, the measured antenna temperature (T_a) is a convolution of the antenna gain pattern with the brightness

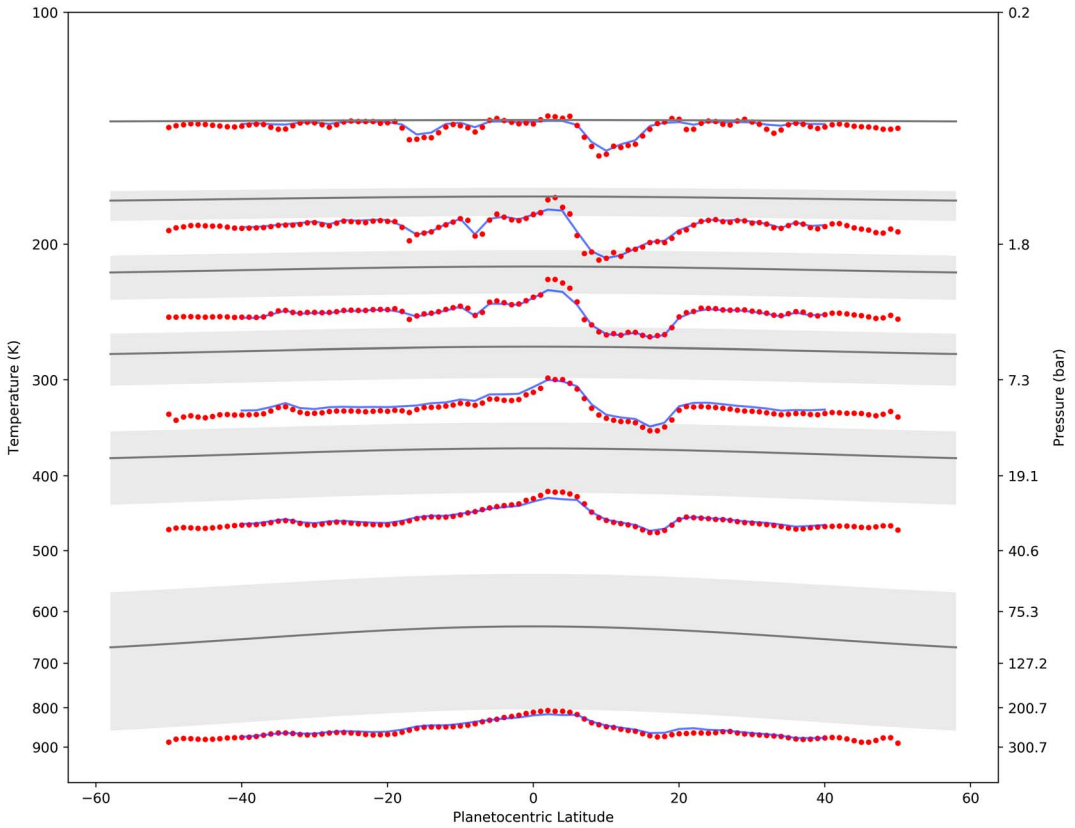

Figure 1. The red dots denote deconvolved nadir brightness temperatures observed by Juno MWR during PJ1. The right axis is the approximate pressure level given by the temperature indicated in the left axis in log scale. Channels 1 to 6 are ordered sequentially from bottom to top. The shaded stripes denote the range of possible nadir brightness temperatures for an ideal adiabatic atmosphere (referenced at 132.1 K at 0.5 bar) with the deep ammonia abundance bounded by Galileo Probe limits, 350 ppm to 782 ppm (566 ppm for the black lines in the center), and the deep water abundance is 0.38%.

temperature, plus calibration error and random instrument noise. At least three kinds of deconvolution algorithms were tested to convert T_a into T_b [*Janssen et al.*, 2017]. Their results agreed with each other within the absolute calibration error. Currently, we focus primarily on the data taken during Juno Perijove 1 (PJ1) at planetocentric latitude range from 40°N to 40°S, and System III longitude from 274°W to 254°W correspondingly, to avoid the possible contamination from synchrotron radiation. Further analysis of high latitudes will be carried out after we gather data from more orbits and gain more knowledge of the synchrotron radiation. The beam footprints on the planet are about 0.5° wide near the equator and grow in size at higher latitudes [*Janssen et al.*, 2017, Figure 20].

In Figure 1, the red dots show the deconvolved nadir brightness temperatures for each channel. The gray strips show the range of possible nadir brightness temperatures for each channel assuming an ideal adiabat and deep ammonia abundance spanning the Galileo Probe Mass Spectrometer (GPMS) limits of 566 ± 216 ppm (9–11 bars) [*Wong et al.*, 2004] (all mixing ratios in this paper refer to volume mixing ratio). The ideal adiabatic atmosphere is dry adiabatic up to the base of the water cloud. The condensation of water releases latent heat, and the temperature profile becomes moist adiabatic within the cloud. Further up, the moist adiabat gradually approaches a dry adiabat, but then it becomes moist adabatic again at the base of the ammonia cloud. The temperature-pressure profile depends on the deep water and ammonia amounts. The brightness temperatures depend mostly on the ammonia abundance, since ammonia is the main opacity source at microwave frequencies. Because the temperature profile is anchored at 0.5 bar, a lower brightness temperature means a higher ammonia abundance, and vice versa. The lowest brightness temperatures observed by channels 1, 2, or 3 barely touch the lower limit of the GPMS's value (350 ppm), while channels 4 and 5 indicate a value within the GPMS's range.

The lowest brightness temperatures occur in a narrow zone at the equator. Elsewhere, the MWR observations show an excess of brightness temperature from what is expected from an ideal adiabatic model using the ammonia abundance range given by GPMS. This positive anomaly suggests a global depletion of ammonia gas relative to its deep abundance, which is consistent with Very Large Array (VLA) observations [*de Pater and Massie*, 1985; *de Pater et al.*, 2001; *de Pater et al.*, 2016]. The VLA observations were limited to a few bars due to synchrotron radiation in the foreground at longer wavelengths, and the MWR observations show that such depletion is much deeper than any pre-Juno expectations, persisting down to 50–60 bars. This discovery challenges the current understanding of Jovian atmospheric dynamics since ammonia condenses at about 0.7 bar and has no known sources or sinks in the atmosphere deeper than the water cloud base. What depletes ammonia to such deep levels is a mystery.

The positive brightness temperature anomaly in the North Equatorial Belt (NEB) at 10–20°N is the other prominent feature in the spectra; it can be interpreted as a significantly low concentration of ammonia. The high brightness temperature in the NEB in channels 5 and 6 is consistent with ground-based observations [*Bjoraker et al.*, 2015; *Fletcher et al.*, 2016]. The largest temperature anomaly is on the southern side of the NEB at shallow depth, and then it gradually shifts to the northern side of the NEB at greater depth. The slope change in the spectra was never expected or observed before. Although the NEB and the South Equatorial Belt (SEB) look similar in both the visible images and the infrared images at 5 μm [*Orton et al.*, 2017], they are very different in the microwave spectrum. The brightness temperature anomaly in the NEB continues to 50–60 bars, while the brightness temperature anomaly in the SEB diminishes at about 10 bars. This huge north-south asymmetry is also not expected.

3. Inversion Method and Results

The principal fact is that ammonia is depleted everywhere down at least to 50–60 bars except near the equator. However, unlike infrared spectroscopy, inversion of the microwave spectra is difficult because the spectral features are nearly absent in the microwave regime. The prevailing method of fitting the microwave spectra is still done manually by forward modeling and trial-and-error to find models that reproduce the data. Here we automate that process using the Markov chain Monte Carlo (MCMC) sampler with Tikhonov regularization to quantitatively fit the spectra and obtain reliable statistics.

3.1. Markov Chain Monte Carlo Algorithm

We model the observation by

$$\widetilde{T}_i = T_i\left(1 + \Delta_{k(i)} + \epsilon_i\right), \tag{1}$$

where $\widetilde{T}_i$ stands for one measurement (realization) of the true brightness temperature T_i and $k(i)$ denotes the channel number for this observation. The two types of Gaussian noise terms, $\Delta_{k(i)}$ and ϵ_i, represent the fractional calibration error, which only depends on the channel number, and the fractional random error, respectively. They have zero means and are independent. The covariance matrix is

$$\Sigma = \mathrm{cov}\left(T_i, T_j\right) = E\left[\left(\widetilde{T}_i - T_i\right)\left(\widetilde{T}_j - T_j\right)\right] = T_i T_j\left(\mathrm{var}(\Delta)\delta_{k(i)k(j)} + \mathrm{var}(\epsilon)\delta_{ij}\right), \tag{2}$$

where δ_{ij} is the Kronecker delta, E is expectation, and var is variance. We have used $E[\Delta_{k(i)}\Delta_{k(j)}] = \mathrm{var}(\Delta)\delta_{k(i)k(j)}$ and $E[\epsilon_i\epsilon_j] = \mathrm{var}(\epsilon)\delta_{ij}$ and $E[\Delta_{k(i)}\epsilon_j] = E[\Delta_{k(j)}\epsilon_i] = 0$ to derive the above equation. The measured brightness temperatures at one place on the planet are collected and sorted such that emission angles come first, then channels. Let the symbol $Y_k = \{T_i \mid I_k \le i < I_{k+1}\}$ represent the true brightness temperatures of channel k, where I_k is the start index of the observations of this channel. $\widetilde{Y} = \left(\widetilde{Y}_1, \widetilde{Y}_2, \ldots, \widetilde{Y}_6\right)^T$ represents the vector of one measurement. Equation (2) shows that the covariance matrix is a block diagonal matrix $\Sigma = \mathrm{diag}(S_1, S_2, \ldots, S_6)$, and each block element S_k is a full matrix:

$$S_k = \begin{pmatrix} T_{I_k}T_{I_k}\left(\mathrm{var}(\Delta) + \mathrm{var}(\epsilon)\right) & T_{I_k}T_{I_k+1}\,\mathrm{var}(\Delta) & \cdots \\ T_{I_k+1}T_{I_k}\,\mathrm{var}(\Delta) & \cdots & \cdots \\ \cdots & \cdots & T_{I_{k+1}-1}T_{I_{k+1}-1}\left(\mathrm{var}(\Delta) + \mathrm{var}(\epsilon)\right) \end{pmatrix} \tag{3}$$

The log probability density function of a multidimensional Gaussian with covariance matrix Σ (rank $r = 6$) is

$$\ln P\left(\widetilde{Y}|Y\right) = -\frac{1}{2}\left(\widetilde{Y}-Y\right)^T \mathrm{diag}(S_1,\ldots,S_6)^{-1}\left(\widetilde{Y}-Y\right) - \frac{r}{2}\ln 2\pi - \frac{1}{2}\ln|\,\mathrm{diag}(S_1,\ldots,S_6)|$$
$$= -\frac{1}{2}\sum_{k=1}^{r}\left[\left(\widetilde{Y}_k - Y_k\right)^T S_k^{-1}\left(\widetilde{Y}_k - Y_k\right) + \ln|S_k| + \ln 2\pi\right] \quad (4)$$

Equation (4) allows a great simplification of calculating the log probability because it means that each channel is independent so that we can calculate the log probability channel by channel and add them together.

Let X represent a generalized state vector that would produce Y through the forward model $Y = F(X)$. The marginal probability of X given the measurement $\widetilde{Y}$, i.e., $P(X|\widetilde{Y})$ is expressed using Bayes' theorem:

$$\ln P\left(X|\widetilde{Y}\right) = \ln P\left(\widetilde{Y}|X\right) + \ln P(X) - \ln P\left(\widetilde{Y}\right) \quad (5)$$

The MCMC algorithm samples $P\left(X|\widetilde{Y}\right)$ by randomly drawing a state (X) from all possible states in the parameter space. If that state satisfies a statistical test, X is added to the Markov chain and a sequence of states is generated according to the principle of detailed balance [*Hastings*, 1970]. The chain will thus converge so that the number density of the states in the chain is proportional to the posterior probability $P\left(X|\widetilde{Y}\right)$.

The final statistics are obtained by gathering all states in the chain. We have used one variation of the general MCMC algorithm, in which a number of chains are advanced simultaneously. The next state of each chain depends on the current states of the other chains. The details of the algorithm are described in *Goodman and Weare* [2010]. This variation allows efficient parallelization of the algorithm.

The log probability derived in equation (4) is generic. Interpreting and assigning values to var(Δ) and var(ϵ) in equation (3) are specific to the retrieval. For the purpose of deriving the deep water abundance, using limb darkening is necessary. As a result, var(Δ) = $(2\%)^2$ and var(ϵ) = $(0.1\%)^2$. On the other hand, the distribution of ammonia can be derived using the nadir brightness temperatures only. The information in the limb darkening is ignored in this study, and each measurement is treated independently, i.e., var(Δ) = 0 and var(ϵ) = $(2\%)^2$.

3.2. Inversion of Jovian Deep Atmospheric Composition

As discussed in section 2, ammonia is depleted at all latitudes down to 50–60 bars except near the equator. We assume that water behaves in the same way. Therefore, the Equatorial Zone (EZ) is a special place on the planet where water and ammonia are uniformly mixed up to the cloud base, with an ideal moist adiabat above. An ideal adiabat can be characterized by three parameters: the deep ammonia abundance, the deep water abundance, and the reference temperature at 0.5 bar. These three parameters determine all the vertical profiles—of temperature, ammonia, and water abundances. We do not consider the formation of NH_4SH cloud because this effect is overwhelmed by other dynamic process such as the evaporation of precipitation (see the discussion in section 4. Strictly speaking, the reference temperature is an upper tie point for the adiabat and is not necessarily the real temperature at 0.5 bar. Because the ideal adiabat is so tightly constrained, we use it to derive a universal temperature profile and the deep ammonia abundance at the EZ, and then apply them to all other latitudes. Thus, the inversion for the ammonia abundance and distribution is done in two stages: the first for the EZ, assuming that it is an ideal adiabat, and the second for all other latitudes, assuming that the temperature profile and the deep ammonia abundance are the same as they are at the equator.

For an ideal adiabat, the parameter space is three dimensional. Deriving a good value for the water abundance requires analysis of limb darkening data. As discussed earlier, results presented here are restricted to the analysis of nadir-viewing data only. Nevertheless, we can test the robustness of the deep dynamical features, as revealed in the ammonia distribution, to an assumed value of the water abundance. Therefore, we run the MCMC algorithm in two dimensions defined by the deep ammonia abundance and the reference temperature, for two different values of deep water abundance. A medium-high water case has H_2O mole fraction of 0.38%, corresponding to O/H = 4.0 times the solar value [*Asplund et al.*, 2009]. A low water case has H_2O mole fraction of 0.06%, corresponding to 0.64 times the solar value.

The prior probability for the deep ammonia abundance is chosen to be uniformly distributed between 0 and 10 times solar abundance. The prior probability for the reference temperature is a Gaussian distribution with a mean of 132.1 K and a standard deviation of 2 K. [*Seiff et al.*, 1998]. Ammonia opacity is modeled according

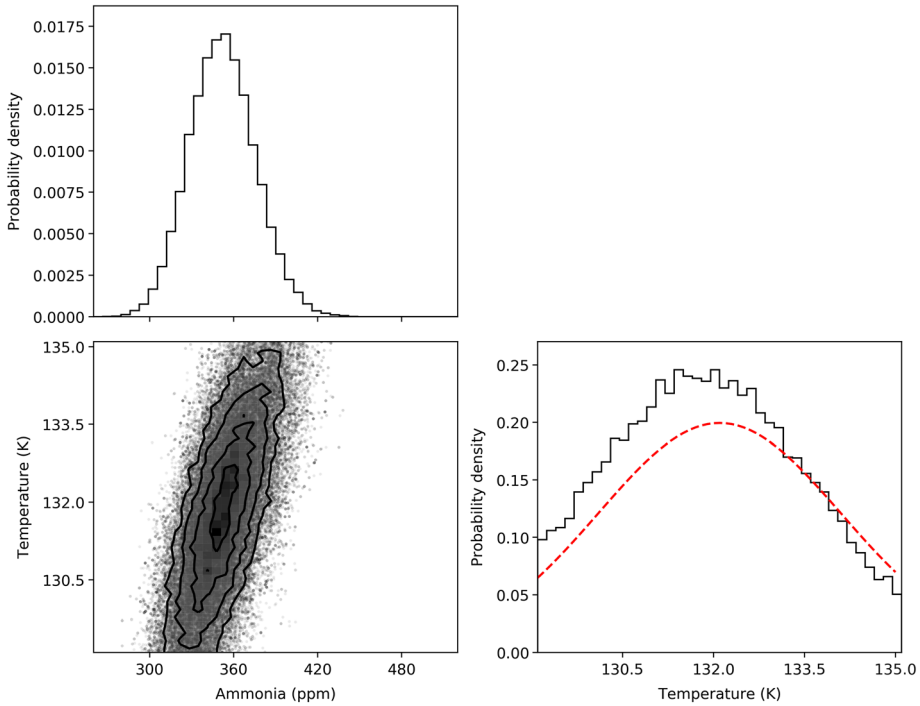

Figure 2. (top and bottom right) Normalized marginal probability density functions for the deep ammonia abundance and the reference temperature at 0.5 bar. The red dashed line shows the prior normal distribution for the reference temperature. (bottom left) Covariance contours between the deep ammonia abundance and the reference temperature. Each dot in the panel is a state in the Markov chain. The density of the dots is proportional to the joint probability of the two parameters.

to *Hanley et al.* [2009]. The estimation of var(ϵ) is increased to $(3\%)^2$ so as to account for the instrument error (2%) [*Janssen et al.*, 2017], the uncertainties resulted from the ammonia opacity model (1%) (based on Figure 1 in *Bellotti et al.* [2016]), and the forward model error resulted from the assumption of ideal adiabat near the equator (2%). The algorithm uses 24 Markov chains with 4000 states in each chain to fit the measured nadir brightness temperature at 2°N. We will express the statistics in the symbol $A^{+\sigma}_{-\delta}$, where $A-\delta$, A, and $A+\sigma$ represent the 16th, 50th, and 84th percentile of the samples in the marginal distribution.

Figure 2 shows the complete probability distribution in three panels for the medium-high water case. The deep ammonia abundance is 351^{+24}_{-23} ppm, and the reference temperature is $131.7^{+1.8}_{-1.8}$ K. The deep ammonia abundance is positively correlated with the reference temperature because the increase of opacity compensates for the increase of temperature. For the low water case, the deep ammonia abundance increases to 373^{+23}_{-23} ppm and the optimal reference temperature increases by 0.5 K. This is because a dry adiabatic atmosphere is warmer than a moist adiabatic one if the temperature is fixed at 0.5 bar. The deep ammonia abundance increases accordingly to lower the brightness temperature. To combine both situations, the overall deep ammonia abundance is estimated to be 362^{+33}_{-33} ppm, equivalent to 2.78 ± 0.25 times the solar abundance.

3.3. Inversion of Jovian Ammonia Profile

The constrained problem of the ideal adiabat applies only to the EZ. At other latitudes one must solve for the vertical profile of ammonia. The problem, which occurs in all profile retrievals from atmospheric sounding, is that the solution of the inversion process is ill-conditioned. Any experimental error in the measurements can be amplified, and the result is a fit to the noise instead of to the signal irrespective of the nonlinear optimization method. *Rodgers* [2000] suggested using a mean value and a standard deviation of the state vector as the prior information to regularize the solution. This method is viable for the remote sounding of Earth's atmosphere because we have prior knowledge of the climatological state of the variable that we are interested in. The Juno MWR is exploring unknown territory, and its major objective is to measure the "climatological"

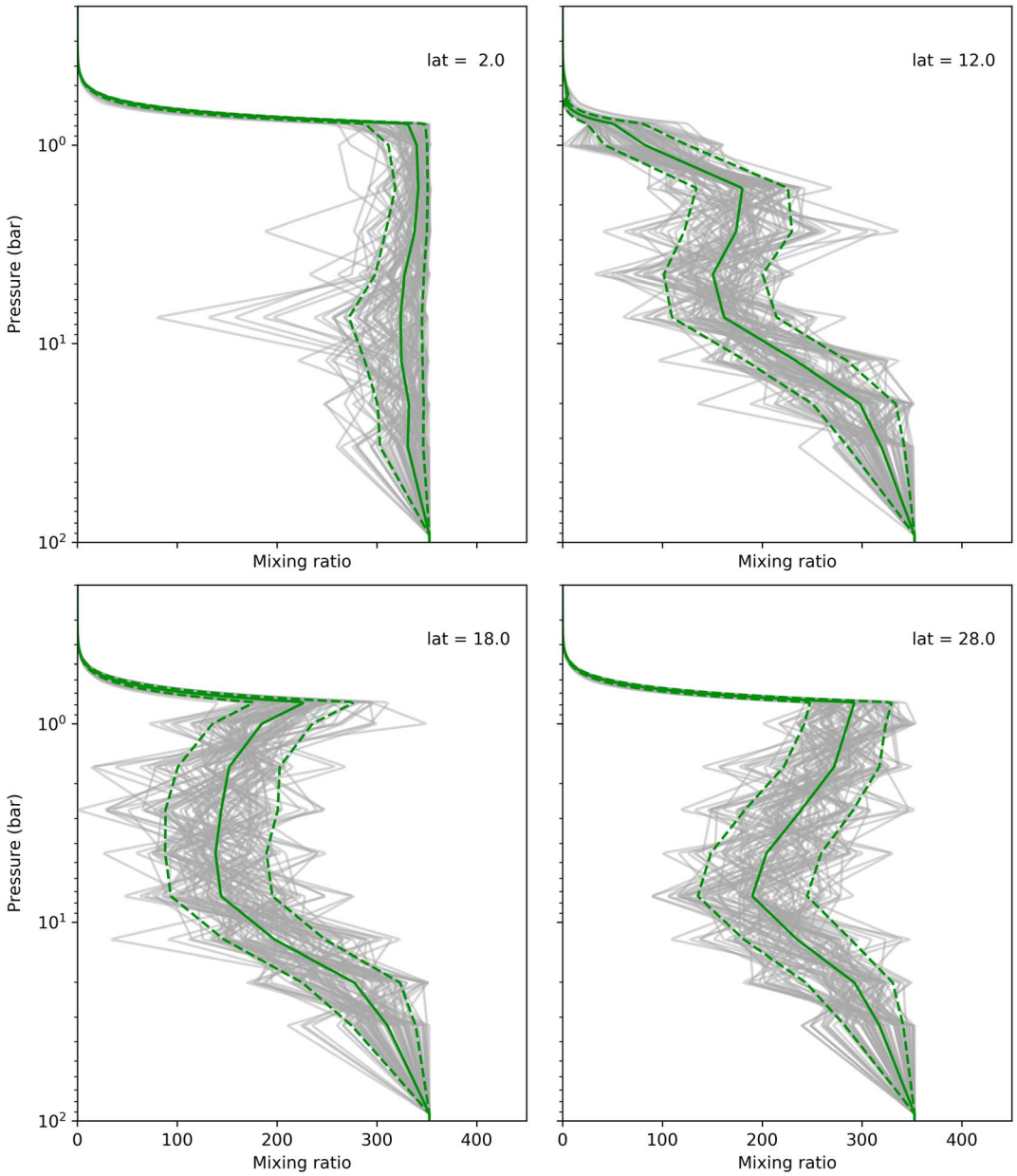

Figure 3. Vertical distribution of ammonia at four typical latitudes: 2°N represents the EZ, 12°N represents the southern branch of the NEB, 18°N represents the northern branch of the NEB, and 28°N represents the extratropics. The gray lines underneath the green ones are 100 randomly sampled ammonia profiles out of 10^6 MCMC simulations. The mean value is the solid green line in each panel, and the 16th and 84th percentiles are shown as the dashed lines.

state of the variable. Rodger's regularization method is less useful in this circumstance. In the next paragraph, we describe the prior knowledge of the state vector and how to impose that in the inversion procedure.

We expect that turbulence and convection will efficiently remove the spatial gradient of ammonia concentration because ammonia has no sources and sinks below the cloud. Therefore, the solution is guided such that (1) it converges on a homogenized atmosphere in the absence of evidence showing that the ammonia has to be inhomogeneous and (2) the ammonia concentration at every level should be equal or less than that in the ideal adiabatic profile. The second point argues that there is no process to enrich ammonia beyond the ideal adiabatic value, which is almost true except in the presence of reevaporation of precipitation. But we keep our model simple at this stage and address that possibility in the later analysis after we gather data from more orbits.

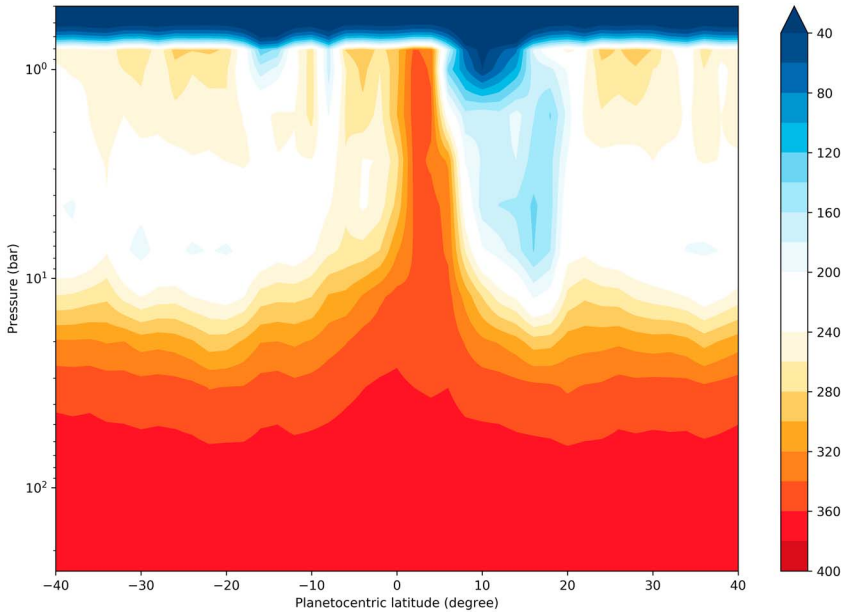

Figure 4. The colored contours show the ammonia concentration in parts per million inverted from nadir brightness temperatures during PJ1 flyby assuming that the deep water abundance is 0.06% (0.65 times solar). The deep ammonia abundance is 373 ppm, and the reference temperature is 132.1 K at 0.5 bar. The aspect ratio in the horizontal and vertical is exaggerated.

The state vector is a set of scaling factors, $X=(x_1, x_2, \ldots, x_n)^T, 0 \le x_i \le 1$, at prescribed pressure levels $p_1, p_2, \ldots, p_n$. The ammonia concentration at pressure p_i is thus $x_i q^*(p_i)$, where $q^*(p_i)$ is the ammonia concentration of an ideal adiabat at pressure p_i. The scaling factor x at any pressure p is given by the linear interpolation of x_i and x_{i+1} on the axis of $\log p_i$ and $\log p_{i+1}$, where $p_i < p < p_{i+1}$. The log probability in equation (5) is modified according to first requirement as

$$\ln P\left(X|\widetilde{Y}\right) = \ln P\left(\widetilde{Y}|X\right) + \ln P(X) - \ln P\left(\widetilde{Y}\right) - \lambda||DX||^2, \tag{6}$$

where λ is a positive tunable parameter describing the strength of regularization and D is the Tikhonov regularization matrix [*Tikhonov et al.*, 1977]:

$$D = \begin{pmatrix} 1 & -1 & 0 & 0 & 0 \\ 0 & 1 & -1 & 0 & 0 \\ 0 & 0 & \ldots & \ldots & 0 \\ 0 & 0 & 0 & 1 & -1 \end{pmatrix} \tag{7}$$

Equation (7) imposes a penalty for large variance of X. If λ is large, the penalty would be large so that the result is guided toward a solution in which X has small variance. We find that $\lambda \approx 1$ balances the goodness of fit and the variances of X. Similar kinds of regularization methods have been used in the hyperspectral imaging of Mars [e.g., *Kreisch et al.*, 2017; *Quemerais et al.*, 2006].

We used the same MCMC sampling algorithm described in section 3.1 according to the log probability expressed in equation (6) with a regularization term in equation (7). The sampling levels are 92.0, 33.1, 20.1, 12.2, 7.39, 4.48, 2.72, 1.65, 1.00, 0.61, and 0.3 bars, each separated by about half a pressure scale height. The scaling factor at the lowest and highest sampling levels are held fixed at 1.0 to satisfy the boundary condition that the ammonia gas is saturated at the top boundary and the ammonia concentration is equal to the deep ammonia abundance at the bottom boundary. Inversions are performed latitude by latitude up to 40° north and south at 2° resolution.

The vertical-latitudinal cross section of ammonia concentration for the medium-high water case is displayed as Figure 3 of *Bolton et al.* [2017]. The profiles of ammonia at four typical latitudes are shown in Figure 3. The EZ (0–5°N) features a high concentration of ammonia of about 350 ppm, which is consistent with the

minimum antenna temperature near the equator in Figure 1. Elsewhere, ammonia is depleted with respect to the deep abundance down to 50 bars, which is consistent with the elevated brightness temperature compared to a baseline ideal adiabatic model. The NEB (5–20°N) has the least amount of ammonia and is divided into two branches. The southern branch is severely depleted in ammonia gas and terminates near 2 bars. The northern branch is moderately depleted in ammonia gas but persists down to 50 bars. This cascade of ammonia abundance is recognized as a slope change in the antenna temperatures versus latitude from channels 1 to 6 in Figure 1. The ammonia concentration in the extratropics has a local minimum near 7 bars, which is robust to 1σ level assuming a conservative 3% error, though the actual error is likely to be less than that [*Janssen et al.*, 2017]. The derived ammonia abundances at the cloud level agree with the Jovian Infrared Auroral Mapper retrievals within measurement uncertainties (Figure 3) [*Orton et al.*, 2017].

The retrieved ammonia distribution for the low water case is displayed in Figure 4. Compared to the medium-high water case, the lapse rate within the water cloud and the temperatures below the water cloud are greater. This forces the ammonia mixing ratio below ~10 bars to be greater as well—by about 25–30 ppm or ~10%. However, the overall structures in the EZ, the NEB, and the extratropics including the ammonia minimum are not changed. The main result of these two cases is that the dynamic features of the deep atmosphere, as revealed by the ammonia distribution, are robust regardless of the choice of water abundance.

4. Conclusions and Discussions

4.1. The Deep Ammonia Abundance

We have assumed that ammonia and water are well mixed below a sufficiently deep level in Jovian atmosphere. Finding a special place on Jupiter that resembles an ideal adiabat allows us to connect the deep abundances to shallow levels where they are measured by the Juno MWR. Figure 1 shows that the EZ is a candidate for such a special place. An ideal adiabat with deep ammonia abundance of 350 ppm matches the measured brightness temperatures of channels 1, 2, and 3 but overestimates those of channels 4 and 5 by about 20 K. This discrepancy suggests that ammonia is more concentrated in the upper atmosphere than the uniformly mixed deep layers, probably due to the reevaporation of precipitated ammonia. The estimated deep ammonia abundance is 362^{+33}_{-33} ppm, just on the lower limit of the GPMS's range and smaller than that suggested by the radio attenuation of the signal from Galileo Probe, which is 700 ± 100 ppm [*Folkner et al.*, 1998].

4.2. The Distribution of Ammonia

The map of ammonia concentration was derived by assuming that there is no lateral temperature gradient on the equipotential surface, because both numerical simulations [e.g., *Kaspi et al.*, 2009; *Schneider and Liu*, 2009] and infrared observations [e.g., *Simon-Miller et al.*, 2006] suggest that lateral temperature differences could be weak (less than 10 K). If a large temperature contrast across equipotential surface are realized, as proposed by *Allison* [2000], they could imply some revision to our preliminary retrieval of the distribution of ammonia. Both the medium-high water case and the low water case show a column of concentrated ammonia gas at the EZ and a global depletion of ammonia down to 50–60 bars. Although the overall structure of the distribution of ammonia is similar to what was shown by Voyager Infrared Interferometer Spectrometer [*Gierasch et al.*, 1986], Cassini Composite Infrared Spectrometer [*Achterberg et al.*, 2006], and ground-based Infrared Telescope Facility Texas Echelon Cross Echelle Spectrograph observations [*Fletcher et al.*, 2016] at the cloud level, the remarkable penetration depth of the depleted ammonia and the cascade of its concentration within the NEB are new discoveries. The choice of the bottom boundary is not consequential as long as it is sufficiently deep because the contribution function of channel 1 is very flat from 100 bars to 1000 bars. If we choose a boundary at deeper levels, the gradient of ammonia concentration from 100 bars to 30 bars is reduced but the column-integrated amount of ammonia should remain approximately unchanged.

Acknowledgments
The research was carried out at the Jet Propulsion Laboratory, California Institute of Technology, under a contract with the National Aeronautics and Space Administration. C.L. was supported by a NASA Earth and Space Science Fellowship and by the NASA Postdoctoral Fellowship. The Juno mission and the team members at JPL were supported by NASA grant NNN12AA01C. We thank all Juno team members for the collaborative efforts. We note that Juno MWR data can be accessed on the Planetary Data System (PDS) https://pds.nasa.gov/.

References

Achterberg, R. K., B. J. Conrath, and P. J. Gierasch (2006), Cassini CIRS retrievals of ammonia in Jupiter's upper troposphere, *Icarus*, *182*(1), 169–180.

Allison, M. (2000), A similarity model for the windy Jovian thermocline, *Planet. Space Sci.*, *48*(7–8), 753–774.

Asplund, M., N. Grevesse, A. J. Sauval, and P. Scott (2009), The chemical composition of the Sun, *Annu. Rev. Astron. Astrophys.*, *47*, 481–522.

Bellotti, A., P. G. Steffes, and G. Chinsomboom (2016), Laboratory measurements of the 5–20 cm wavelength opacity of ammonia, water vapor, and methane under simulated conditions for the deep Jovian atmosphere, *Icarus*, *280*, 255–267.

Bjoraker, G. L., M. H. Wong, I. de Pater, and M. Adamkovics (2015), Jupiter's deep cloud structure revealed using keck observations of spectrally resolved line shapes, *Astrophys. J.*, *810*(2).

Bolton, S., et al. (2017), Jupiter's interior and deep atmosphere: The first close polar pass with the Juno spacecraft, *Science*, doi:10.1126/science.aal2108, in press.

de Pater, I., and S. T. Massie (1985), Models of the millimeter-centimeter spectra of the Giant planets, *Icarus*, *62*(1), 143–171.

de Pater, I., D. Dunn, P. Romani, and K. Zahnle (2001), Reconciling Galileo probe data and ground-based radio observations of ammonia on Jupiter, *Icarus*, *149*(1), 66–78.

de Pater, I., R. J. Sault, B. Butler, D. DeBoer, and M. H. Wong (2016), Peering through Jupiter's clouds with radio spectral imaging, *Science*, *352*(6290), 1198–1201.

Fletcher, L. N., T. Greathouse, G. Orton, J. Sinclair, R. Giles, P. Irwin, and T. Encrenaz (2016), Mid-infrared mapping of Jupiter's temperatures, aerosol opacity and chemical distributions with IRTF/TEXES, *Icarus*, *278*, 128–161.

Folkner, W. M., R. Woo, and S. Nandi (1998), Ammonia abundance in Jupiter's atmosphere derived from the attenuation of the Galileo probe's radio signal, *J. Geophys. Res.*, *103*(E10), 22,847–22,855, doi:10.1029/98JE01635.

Gierasch, P. J., B. J. Conrath, and J. A. Magalhaes (1986), Zonal mean properties of Jupiter upper troposphere from Voyager infrared observations, *Icarus*, *67*(3), 456–483.

Goodman, J., and J. Weare (2010), Ensemble samplers with affine invariance, *Commun. Appl. Math. Comput. Sci.*, *5*(1), 65–80.

Hanley, T. R., P. G. Steffes, and B. M. Karpowicz (2009), A new model of the hydrogen and helium-broadened microwave opacity of ammonia based on extensive laboratory measurements, *Icarus*, *202*(1), 316–335.

Hastings, W. K. (1970), Monte-Carlo sampling methods using Markov chains and their applications, *Biometrika*, *57*(1), 97–109.

Janssen, M., J. Oswald, S. Brown, S. Gulkis, S. Levin, S. Bolton, M. Allison, S. Atreya, D. Gautier, and A. Ingersoll (2017), MWR: Microwave radiometer for the Juno mission to Jupiter, *Space Sci. Rev.*, 1–47.

Kaspi, Y., G. R. Flierl, and A. P. Showman (2009), The deep wind structure of the giant planets: Results from an anelastic general circulation model, *Icarus*, *202*(2), 525–542.

Kreisch, C. D., J. A. O'Sullivan, R. E. Arvidson, D. V. Politte, L. He, N. T. Stein, J. Finkel, E. A. Guinness, M. J. Wolff, and M. G. A. Lapotre (2017), Regularization of Mars Reconnaissance Orbiter CRISM along-track oversampled hyperspectral imaging observations of Mars, *Icarus*, *282*, 136–151.

Orton, G. S., et al. (2017), Multiple-wavelength sensing of Jupiter during the Juno mission's first Perijove passage, *Geophys. Res. Lett.*, doi:10.1002/2017GL073019, in press.

Quemerais, E., J. L. Bertaux, O. Korablev, E. Dimarellis, C. Cot, B. R. Sandel, and D. Fussen (2006), Stellar occultations observed by SPICAM on Mars express, *J. Geophys. Res.*, *111*, E09S04, doi:10.1029/2005JE002604.

Rodgers, C. D. (2000), *Inverse Methods for Atmospheric Sounding: Theory and Practice*, pp. 159–173, World Scientific Publ.

Schneider, T., and J. J. Liu (2009), Formation of jets and equatorial superrotation on Jupiter, *J. Atmos. Sci.*, *66*(3), 579–601.

Seiff, A., D. B. Kirk, T. C. D. Knight, R. E. Young, J. D. Mihalov, L. A. Young, F. S. Milos, G. Schubert, R. C. Blanchard, and D. Atkinson (1998), Thermal structure of Jupiter's atmosphere near the edge of a 5-mu m hot spot in the north equatorial belt, *J. Geophys. Res.*, *103*(E10), 22,857–22,889, doi:10.1029/98JE01766.

Simon-Miller, A. A., B. J. Conrath, P. J. Gierasch, G. S. Orton, R. K. Achterberg, F. M. Flasar, and B. M. Fisher (2006), Jupiter's atmospheric temperatures: From Voyager IRIS to Cassini CIRS, *Icarus*, *180*(1), 98–112.

Tikhonov, A. N., V. I. A. K. Arsenin, and F. John (1977), *Solutions of Ill-Posed Problems*, pp. 45–94, Winston, Washington, D. C.

Wong, M. H., P. R. Mahaffy, S. K. Atreya, H. B. Niemann, and T. C. Owen (2004), Updated Galileo probe mass spectrometer measurements of carbon, oxygen, nitrogen, and sulfur on Jupiter, *Icarus*, *171*(1), 153–170.